

Epitaxial stannate pyrochlore thin films: Limitations of cation stoichiometry and electron doping

Cite as: APL Mater. 9, 051113 (2021); doi: 10.1063/5.0049334

Submitted: 3 March 2021 • Accepted: 14 April 2021 •

Published Online: 12 May 2021



View Online



Export Citation



CrossMark

Felix V. E. Hensling,^{1,a)} Diana Dahliah,² Prabin Dulal,^{3,4} Patrick Singleton,⁵ Jiaxin Sun,¹ Jürgen Schubert,⁶ Hanjong Paik,^{1,5} Indra Subedi,^{3,4} Biwas Subedi,^{3,4} Gian-Marco Rignanese,² Nikolas J. Podraza,^{3,4} Geoffrey Hautier,^{2,7} and Darrell C. Schlom^{1,8,9}

AFFILIATIONS

¹ Department of Materials Science and Engineering, Cornell University, Ithaca, New York 14853, USA

² Institute of Condensed Matter and Nanosciences, Université catholique de Louvain, 1348 Louvain-la-Neuve, Belgium

³ Department of Physics and Astronomy, University of Toledo, Toledo, Ohio 43606, USA

⁴ Wright Center for Photovoltaics Innovation and Commercialization, University of Toledo, Toledo, Ohio 43606, USA

⁵ Platform for the Accelerated Realization, Analysis, and Discovery of Interface Materials (PARADIM), Cornell University, Ithaca, New York 14853, USA

⁶ Peter Grünberg Institute (PGI9-IT), JARA-Fundamentals of Future Information Technology, Forschungszentrum Jülich GmbH, Jülich 52425, Germany

⁷ Thayer School of Engineering, Dartmouth College, Hanover, New Hampshire 03755, USA

⁸ Kavli Institute at Cornell for Nanoscale Science, Ithaca, New York 14853, USA

⁹ Leibniz-Institut für Kristallzüchtung, Max-Born-Strasse 2, 12849 Berlin, Germany

^{a)} Author to whom correspondence should be addressed: hensling@cornell.edu

ABSTRACT

We have studied the growth of epitaxial films of stannate pyrochlores with a general formula $A_2\text{Sn}_2\text{O}_7$ ($A = \text{La}$ and Y) and find that it is possible to incorporate $\sim 25\%$ excess of the A -site constituent; in contrast, any tin excess is expelled. We unravel the defect chemistry, allowing for the incorporation of excess A -site species and the mechanism behind the tin expulsion. An A -site surplus is manifested by a shift in the film diffraction peaks, and the expulsion of tin is apparent from the surface morphology of the film. In an attempt to increase $\text{La}_2\text{Sn}_2\text{O}_7$ conductivity through n -type doping, substantial quantities of tin have been substituted by antimony while maintaining good film quality. The sample remained insulating as explained by first-principles computations, showing that both the oxygen vacancy and antimony-on-tin substitutional defects are deep. Similar conclusions are drawn on $\text{Y}_2\text{Sn}_2\text{O}_7$. An alternative n -type dopant, fluorine on oxygen, is shallow according to computations and more likely to lead to electrical conductivity. The bandgaps of stoichiometric $\text{La}_2\text{Sn}_2\text{O}_7$ and $\text{Y}_2\text{Sn}_2\text{O}_7$ films were determined by spectroscopic ellipsometry to be 4.2 eV and 4.48 eV, respectively.

© 2021 Author(s). All article content, except where otherwise noted, is licensed under a Creative Commons Attribution (CC BY) license (<http://creativecommons.org/licenses/by/4.0/>). <https://doi.org/10.1063/5.0049334>

I. INTRODUCTION

The potpourri of interesting and useful properties exhibited by transition metal oxides has resulted in extensive studies on this class of materials over the years.¹ Oxides with a general formula $A_2B_2O_6O'$ (commonly abbreviated to $A_2B_2O_7$), where A and B are metals and O and O' are two different oxygen sites, belong to

a family of structures referred to as pyrochlores. Pyrochlores are particularly interesting as they themselves exhibit a wide variety of physical properties, which are based on the extensive combination of A -site (rare earth or inert lone-pair electron element) and B -site (transition or post-transition metal) cations with oxygen.^{2,3} Consequently, their potential applications are numerous. Examples include tunable dielectrics,⁴⁻⁷ dielectrics with high

radiation tolerance,^{8,9} catalysts,^{10–12} and novel materials for information technology applications.^{13,14}

$\text{La}_2\text{Sn}_2\text{O}_7$ is a particularly interesting pyrochlore. It has been shown to be photoluminescent¹⁵ and highly radiation tolerant.⁹ It is further a promising catalyst, e.g., for catalytic methane combustion^{16–18} and photocatalysis.^{19–21}

Epitaxial thin films provide excellent model systems for understanding catalysis. This is because they enable the effect of crystalline orientation on catalysis to be studied on large-area surfaces. Furthermore, epitaxy enables the purposeful introduction of defects and the engineering of strain. Ultimately, the epitaxial film approach allows the surface of the catalyst to be different from its underlying support, making it possible to separately optimize the structure and composition of each for higher-performance oxide catalysts that are designed at the atomic-layer level.^{22–24}

For $\text{La}_2\text{Sn}_2\text{O}_7$ specifically, previous studies of the catalytic activity for the combustion of methane have found that additional oxygen vacancies induced by cation doping are beneficial.¹⁷ An approach to avoid an external dopant and, thus, an additional parameter that can influence the catalytic activity is to exploit the adjustable cation stoichiometry available by epitaxy, which can potentially yield oxygen vacancies.²⁵

Doping $\text{La}_2\text{Sn}_2\text{O}_7$ is not only an effective way to increase its (photo-)catalytic activity,^{17,21} but for certain dopants, it is also predicted to yield *n*-type conductivity, resulting in a transparent conducting oxide.^{14,15,26} Achieving *n*-type conductivity would also endow $\text{La}_2\text{Sn}_2\text{O}_7$ with the prerequisite characteristics, enabling a bilayer structure that is predicted to yield a novel superconductor to be synthesized and experimentally assessed. The specific interface structure predicted involves coupling spin-ice fluctuations from a quantum spin-ice with a conductor having a single isotropic Fermi surface pocket to drive topological odd-parity pairing at the interface between the quantum spin-ice and the electrical conductor.¹⁴ Quantum spin-ices are (so far) exclusively found in pyrochlores, so considering the requirements for the conducting part of the heterostructure and that it needs to form a high-quality interface with a quantum spin-ice, *n*-type doped $\text{La}_2\text{Sn}_2\text{O}_7$ is one of the few ideal candidates.

Despite the interesting properties and applications of $\text{La}_2\text{Sn}_2\text{O}_7$, there are, to our knowledge, no reports of its preparation in the form of epitaxial thin films. In this article, we provide a guide to the growth of high-quality epitaxial $\text{La}_2\text{Sn}_2\text{O}_7$ thin films by means of molecular-beam epitaxy (MBE). We explore the limits of cation non-stoichiometry in $\text{La}_2\text{Sn}_2\text{O}_7$ thin films and discuss the underlying mechanisms and resulting defect structures. We unravel the challenge of achieving electronic conductivity in $\text{La}_2\text{Sn}_2\text{O}_7$. First-principles point-defect computations show that potential electron donors such as oxygen vacancies or the substitution of antimony for tin are too deep within the bandgap to lead to significant conductivity. We also show that these results can be equally applied to $\text{Y}_2\text{Sn}_2\text{O}_7$, which is known for its luminescence,^{27,28} has promising photo-catalytic properties,²⁹ and, if electronic conductivity can be achieved, is another candidate for the aforementioned superconducting heterostructure.¹⁴ It is thus likely that these results can be generally applied to the epitaxial growth of stannate pyrochlores.

II. EXPERIMENTAL

All thin films are grown on (111)-oriented yttria-stabilized zirconia (YSZ) substrates from CrysTec GmbH. X-ray diffraction (XRD) obtained with a Panalytical Empyrean with $\text{Cu-K}\alpha_1$ radiation reveals a substrate lattice constant of $a = 0.515$ nm. As both pyrochlores, $\text{La}_2\text{Sn}_2\text{O}_7$ ($a = 1.0703$ nm)³⁰ and $\text{Y}_2\text{Sn}_2\text{O}_7$ ($a = 1.0372$ nm),³¹ have a cubic lattice constant nearly double that of YSZ, the expected in-plane mismatches for the ideal stoichiometry are -3.8% and -0.7% , respectively. The thin films are grown in a Veeco Gen10 MBE at a background pressure of 10^{-6} Torr of $\sim 10\%$ distilled ozone and 90% oxygen. The growth temperature of 700°C is measured by using a thermocouple and an optical pyrometer at a measurement wavelength of 980 nm. The fluxes emanating from molecular beams of the constituent A-site cations, yttrium and lanthanum, are measured by using a quartz crystal micro-balance (QCM). The flux emanating from an SnO_2 source is also measured by using a QCM, assuming that the species in the molecular beam are mainly SnO .^{32–34} The ratio between the fluxes is varied by changing the temperatures of the effusion cells that contain lanthanum, yttrium, and SnO_2 . The growth is monitored in real time by reflection high-energy electron diffraction (RHEED), and the surface morphology is measured by using an Asylum Research Cypher ES atomic force microscope (AFM).

The electronic structure and the formation energy of point defects were calculated using density functional theory (DFT) adopting the projector augmented wave (PAW) method,³⁵ as implemented in the Vienna *Ab initio* Simulation Package (VASP).^{36,37} The wavefunctions were expanded on a plane-wave basis set employing a cutoff energy of 520 eV. The atomic coordinates and the vector lattice were fully optimized. The point defects were studied using the supercell approach.³⁸ The different atomic models were generated utilizing the Python Charge Defects Toolkit (PyCDT)³⁹ using a supercell of 88 atoms. The Brillouin zone was sampled using a Γ only *k*-point grid. The exchange–correlation (XC) potential was obtained through adopting the Heyd–Scuseria–Ernzerhof (HSE) hybrid functional with an exact-exchange fraction of 0.25 and a screening length of 0.2 Å.^{40,41} Spin-polarized calculations were performed, and all supercells were relaxed at fixed volume until the forces on the ions were smaller than 0.1 eV/Å. The occupation of the electronic states was determined through the Gaussian smearing method with a smearing width of 0.05 eV. The formation energy of each charged-defect state was computed as a function of the Fermi level E_f as^{42,43}

$$E_{\text{form}}[X^q, E_f] = E_{\text{tot}}[X^q] - E_{\text{tot}}^{\text{bulk}} - \sum n_i \mu_i + qE_f + E_{\text{corr}}, \quad (1)$$

where $E_{\text{tot}}[X^q]$ and $E_{\text{tot}}^{\text{bulk}}$ are the total energies of the defective supercell (for a given defect *X* in the charge state *q*) and the bulk energy, respectively. The third term represents the energy needed to exchange atoms with thermodynamic reservoirs, where n_i indicates the number of atoms of the species *i* removed or added to create the defect, and μ_i are the corresponding chemical potentials. We computed the phase diagram of La–Sn–F–Sb and La–Sn–O–Sb at 0 K at the same level of theory from the phases (La, Sb, O_2 , Sn, F_2 , LaSn_3 , SnO_2 , La_3Sn , SnO , La_2O_3 , $\text{La}_2\text{Sn}_2\text{O}_7$, La_5Sn_3 , Sn_5O_6 , LaSn , La_3Sn_7 , La_2Sn_3 , LaSbO_4 , La_3SbO_7 , LaF_3 , LaOF) and determined the limits of the allowed chemical potential of these species. The fourth

term represents the energy to exchange electrons with the host material through the electronic chemical potential, which is the Fermi energy level E_f . Finally, the last term in the equation, $E_{corr.}$, is a correction accounting for the finite size of the supercell, as well as potential-alignment corrections to restore the position of the pure bulk valence band maximum (VBM) in charged-defect calculations due to the presence of the compensating background charge density. Here, we used extended Freysoldt's (Kumagai's) scheme.^{44,45} The thermodynamic transition state of defect X from state q_1 to q_2 , which corresponds to the energy level at which a defect captures (or emits) a free carrier, is defined as the position of the Fermi level at which the defect formation energy of both states q_1 and q_2 is equal ($E_{form}[X^{q_1}, E_f] = E_{form}[X^{q_2}, E_f]$). The transition level, $\epsilon(q_1/q_2)$, relative to the VBM (i.e., $E_f = E_{VBM}$) is

$$\epsilon(q_1/q_2) = \frac{E_{form}[X^{q_2}, E_{VBM}] - E_{form}[X^{q_1}, E_{VBM}]}{q_2 - q_1}. \quad (2)$$

Spectroscopic ellipsometry measurements of $\text{La}_2\text{Sn}_2\text{O}_7$ and $\text{Y}_2\text{Sn}_2\text{O}_7$ epitaxial thin films were performed using a single rotating compensator multichannel ellipsometer (M-2000, J.A Woolam Co.) at an angle of incidence of 70° over a photon energy range from 0.74 to 5.89 eV.^{46,47} The complex dielectric function ($\epsilon = \epsilon_1 + i\epsilon_2$) spectra and structural parameters of the films including film and surface roughness layer thicknesses were determined from the measured ellipsometric spectra using divided spectral range analysis.^{48,49} The structural models of the samples consisted of a semi-infinite YSZ substrate, epitaxial thin film, and surface roughness. The optical properties of the YSZ substrate were also obtained from divided spectral range analysis. The optical response of the surface roughness was represented by the Bruggeman effective medium approximation,^{50,51} which consists of equal parts of the top material (YSZ, $\text{La}_2\text{Sn}_2\text{O}_7$, or $\text{Y}_2\text{Sn}_2\text{O}_7$) and void.

III. LIMITS OF CATION NON-STOICHIOMETRY IN $\text{La}_2\text{Sn}_2\text{O}_7$

Varying the cation ratios allows us to find the point of ideal cation stoichiometry and to further establish limits of non-stoichiometry for the targeted phases. A first assessment of the influence of the Sn/La ratio variation on the crystallinity and surface quality of the $\text{La}_2\text{Sn}_2\text{O}_7$ thin films can be made by monitoring the real-time RHEED pattern along the $[1\bar{1}0]$ azimuth of both the film and the substrate. We expect $\bar{1}0$ and 10 streaks of the epitaxial $\text{La}_2\text{Sn}_2\text{O}_7$ film to appear at the half-order positions of the (111) YSZ substrate. This is because a $\text{La}_2\text{Sn}_2\text{O}_7$ film with the pyrochlore structure has a cubic lattice constant nearly double that of the YSZ substrate. Observing the RHEED pattern during growth, three different types of patterns emerge.

The first type of RHEED pattern is observed when the lanthanum surplus is so high that the Sn/La ratio is less than or equal to 0.58. A representative pattern of this type is shown in Fig. 1(a). The expected $\bar{1}0$ and 10 streaks of epitaxial $\text{La}_2\text{Sn}_2\text{O}_7$ are practically invisible. Nonetheless, it shows narrow streaks indicative of the growth of a cubic epitaxial structure. Additionally, a diffuse background signal can be observed, which indicates significant amorphous content.

The second type of RHEED pattern is found for depositions with less lanthanum-excess, all the way up to the stoichiometric ratio of Sn/La, i.e., $0.74 \leq \text{Sn/La} \leq 1$. A representative RHEED pattern is shown in Fig. 1(b). The $\bar{1}0$ and 10 streaks are now clearly visible in the positions expected for epitaxial $\text{La}_2\text{Sn}_2\text{O}_7$ marked by the white arrows, and all streaks are sharp, indicative of high crystalline quality.

Increasing the tin ratio further results in a decrease in diffraction intensity until a La/Sn ratio of 1.33 or more is supplied. Figure 1(c) shows a representative RHEED pattern of this type. The intensity is markedly lower than for the other La/Sn ratios, leaving the streaks expected for a cubic epitaxial structure (marked by arrows) barely visible. Additionally, spots emerge along faintly visible diffraction rings (marked for better visibility). The rings indicate polycrystalline growth, and the spots indicate the formation of islands.

In order to understand the three types of RHEED patterns, it is helpful to consider the associated surface morphologies. The bottom row of Fig. 1 shows representative $1 \times 1 \mu\text{m}^2$ surface morphology scans from the corresponding films on which the RHEED patterns in the top row were taken. Starting with the highly lanthanum-rich growth conditions, the surface morphology in Fig. 1(d) contains islands, which are probably responsible for the diffuse RHEED signal. Nevertheless, the underlying step structure is still clearly visible, and with an rms value of 0.7 nm, the surface is relatively smooth. The morphology of samples grown under less lanthanum-excess, $0.74 \leq \text{Sn/La} \leq 1$ [Fig. 1(e)], are atomically smooth (rms ≈ 0.2 nm) and, thus, in good agreement with the associated RHEED pattern. The RHEED patterns of samples grown under tin-rich conditions indicate a loss of the single crystallinity of the surface. This is consistent with the surface morphology seen in Fig. 1(f). It reveals densely packed islands, and atomic steps are no longer visible. The surface is significantly rougher (rms ≈ 3.1 nm) than the other two cases.

While RHEED and AFM allow us to define three different growth regimes with distinct features, the surface sensitivity of both techniques does not provide a measure of the bulk crystallinity of the films. This can be achieved, however, by XRD. Figures 2(a) and 2(b) show XRD patterns for films with varying cation ratios shifted along the y axis for clarity.

θ - 2θ XRD scans of the $\text{La}_2\text{Sn}_2\text{O}_7$ films deposited at different Sn/La ratios are shown in Fig. 2(a). The expected 2θ values based on the lattice constant of bulk $\text{La}_2\text{Sn}_2\text{O}_7$ are marked by the dashed lines.³⁰ To analyze the diffraction data, it is again helpful to divide the data into three types of patterns. Starting with the highly lanthanum-rich-type represented by the diffraction pattern of the films grown at Sn/La = 0.58 in purple, we note that the expected 111 and 333 peaks of $\text{La}_2\text{Sn}_2\text{O}_7$ are missing. Nonetheless, peaks close to the expected 222 and 444 peak positions can be observed. These peaks are noticeably shifted to lower diffraction angles, and the shift is most recognizable for the 444 peak. For less lanthanum-rich (blue Sn/La = 0.74 and turquoise Sn/La = 0.93) and stoichiometric (pink) growth conditions, all expected peaks in the 2θ range from 10° to 70° are observed, with the diffraction peaks with odd indices being less intense than those with even indices. This observed intensity difference is in agreement with the observed intensities from powder diffraction, 222 being the most intense followed by 444, 333 being significantly less intense, and finally 111 showing the least

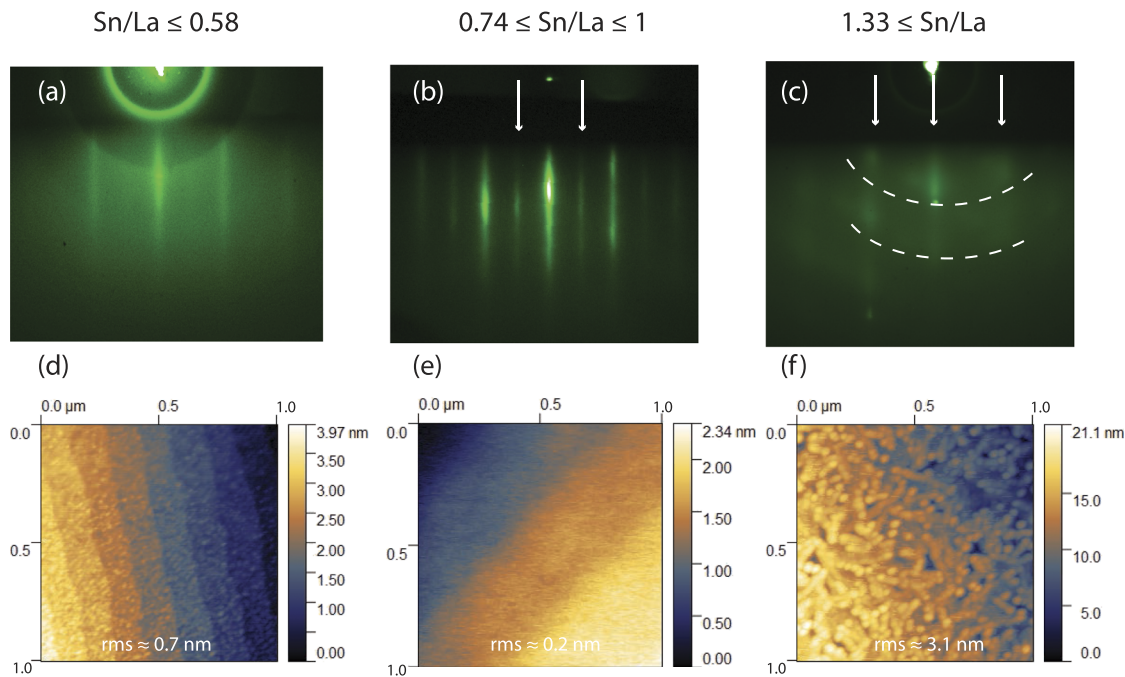


FIG. 1. (a)–(c) Representative RHEED patterns with the electron beam incident along the $[1\bar{1}0]$ azimuth of both the film and the substrate. (d)–(f) Surface morphologies of the corresponding ~ 30 nm thick films including rms roughness resulting from $\text{Sn/La} \leq 0.58$ (left column), $0.74 \leq \text{Sn/La} \leq 1$ (central column), and $1.33 \leq \text{Sn/La}$ (right column). (a) A heavily lanthanum-rich growth results in a streaky RHEED pattern with diffuse background; the associated surface morphology shown in (d) reveals the formation of comparably small islands, while the step structure remains visible. (b) In the less tin deficient to stoichiometric supply regime, the RHEED pattern expected for epitaxial pyrochlore $\text{La}_2\text{Sn}_2\text{O}_7$ is observed with clear $\bar{1}0$ and 10 streaks marked by arrows. The resulting morphology in (e) is atomically smooth. (c) A surplus of supplied tin results in a RHEED pattern with barely visible cubic reflections (marked by arrows), spots, and rings (marked by dashed lines). The corresponding surface morphology (f) is comparably rough; note that the color scheme of the scale bar of each image is different.

intensity.³⁰ The red pattern is observed for the sample grown with a Sn/La ratio of 1.33. Here, the 222, 333, and 444 peaks are observed at the expected angles, while the 111 peak is missing.

The differences among the diffraction patterns are also apparent when we take a closer look at the most intense $\text{La}_2\text{Sn}_2\text{O}_7$ 222 peak next to the YSZ 111 peak. Figure 2(b) shows the diffraction pattern of the $\text{La}_2\text{Sn}_2\text{O}_7$ 222 peak. Two observations are immediately apparent. The first is that all patterns except that from the Sn/La = 1.33 sample show clear thickness fringes, signs of the good crystallinity, and smooth surfaces. Second, a shift of the 222 peak is visible. Beginning with the film grown with the most lanthanum surplus (purple), the 2θ position of the 222 peak is seen to shift from lower angles toward the bulk value, reaching it at the stoichiometric point (pink). A tin-rich growth results in a comparably small peak shift toward lower angles (red). Furthermore, the reciprocal space map of the 331 substrate peak and the 662 film peak of the Sn/La = 1 sample in Fig. 2(c) reveals that the film is fully relaxed.

Figure 3(a) illustrates the influence of supplying different Sn/La ratios (red) during growth on the crystal structure by showing the out-of-plane lattice constant. The out-of-plane lattice constant is determined from the 222 peak position shown in Fig. 2(b). As expected from the dependence of the peak shift of the 222 peak on the Sn/La ratio, the out-of-plane lattice constant is the highest for the most lanthanum-rich sample. As the Sn/La ratio approaches the stoichiometric value, the out-of-plane lattice

constant approaches the bulk value, which is expected for fully relaxed films. For tin-rich growth, the out-of-plane lattice constant increases only slightly. Interestingly, no influence of the cation stoichiometry on the FWHM of the rocking curves shown in Fig. 3(c) was detectable; it was rather governed by the substrate quality and below 0.02° for all $\text{La}_2\text{Sn}_2\text{O}_7$ films. The lack of influence of stoichiometry on the symmetric rocking curve peak has been noted in some other oxide systems, e.g., $\text{Sr}_{1+\delta}\text{TiO}_{3+x}$,^{52,53} $\text{La}_{1+\delta}\text{AlO}_{3+x}$,⁵⁴ and $\text{La}_{1+\delta}\text{CrO}_{3+x}$,⁵⁵ whereas it is not the case for $\text{Ba}_{1+\delta}\text{SnO}_{3+x}$,⁵⁶ hexagonal $\text{Lu}_{1+\delta}\text{FeO}_{3+x}$,⁵⁷ or $\text{Pb}_{1+\delta}\text{TiO}_{3+x}$.⁵⁸

Figure 3(b) shows the representative off-axis ϕ -scans of the most tin-rich (red), the stoichiometric (pink), and the lanthanum-rich sample (purple). As all films show the same three-fold symmetry as the substrate (black), the cube-on-cube epitaxial relationship between films and respective YSZ substrates is confirmed.

Considering the surface crystallinity and morphology and correlating them with the structural information allow us to define three growth regimes and their characteristics:

Regime I: For Sn/La ratios between 0.74 and 1, the surfaces are atomically flat and the RHEED pattern reveals high-quality crystalline growth. The XRD pattern also shows all expected peaks. With an increase in lanthanum, the out-of-plane film peaks shift to lower 2θ angles. This regime defines the growth window for high-quality epitaxial $\text{La}_2\text{Sn}_2\text{O}_7$ with the pyrochlore structure.

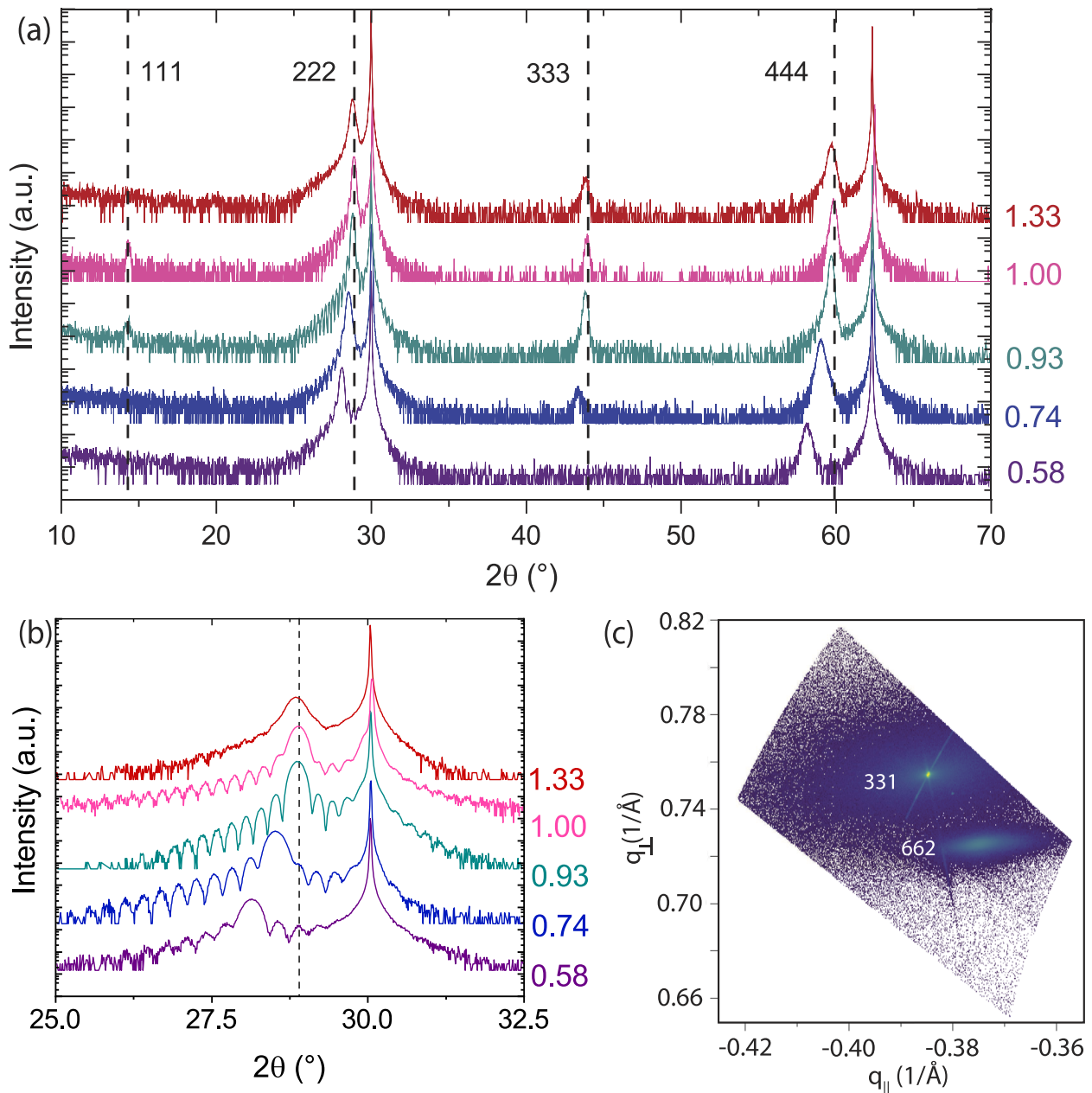


FIG. 2. θ - 2θ x-ray diffraction scans of ~ 30 nm thick films grown with different Sn/La ratios [given by the numbers on the right-hand side of (a) and (b)]. (a) Wide-range scan between $2\theta = 10^\circ$ and $2\theta = 70^\circ$ and (b) narrow-range scan in the vicinity of the $\text{La}_2\text{Sn}_2\text{O}_7$ 222 peak next to the YSZ 111 peak. The dashed lines mark the expected diffraction angles of $\text{La}_2\text{Sn}_2\text{O}_7$ based on the bulk lattice constant.³⁰ (c) Reciprocal space map of the 331 substrate peak and the 662 film peak of a film with a cation ratio of 1, revealing that the film is fully relaxed.

Regime II: For Sn/La ratios of 0.58 or lower, the RHEED pattern becomes significantly more diffuse. The surface morphology reveals the formation of islands, while atomic steps remain visible. Both the 111 and 333 peaks are missing from the diffraction pattern in this regime. The shift of the 222 peak, however, still follows the trend of the peak shift observable in regime I for an increase in

lanthanum. The ϕ -scan and RHEED pattern both reveal the epitaxial nature of the films in this regime.

Regime III: For films grown under tin-rich conditions ($1.33 \leq \text{Sn/La}$), the RHEED pattern indicates a mixture of polycrystalline and amorphous surface phases. The surface morphology is expectedly rough. It is, thus, also not surprising that no thickness

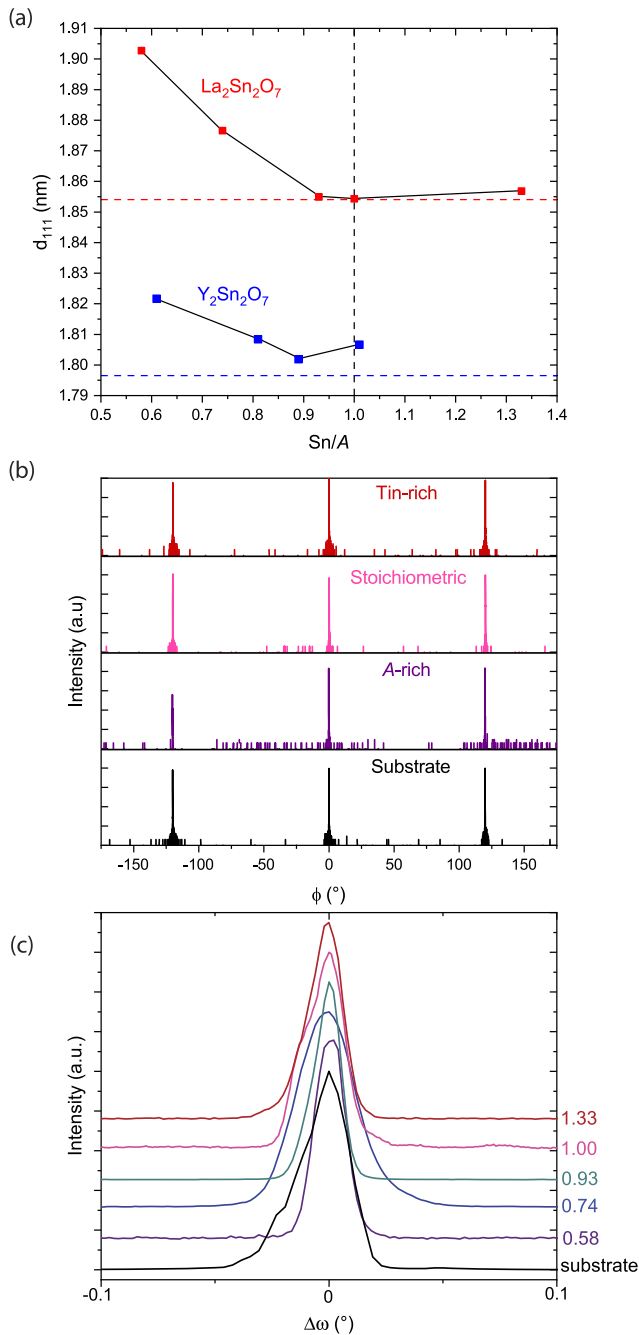
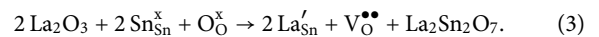


FIG. 3. (a) Out-of-plane lattice constants (left axis) of $\text{La}_2\text{Sn}_2\text{O}_7$ (red) and $\text{Y}_2\text{Sn}_2\text{O}_7$ (blue) determined from the peak positions in Figs. 2(b) and 8(a), respectively, as a function of the supplied cation ratios during growth. The line connecting the data points is a guide to the eye. The dashed lines mark the stoichiometric cation ratio and the bulk out-of-plane lattice constant, respectively. (b) Representative off-axis ϕ -scans of the 400 family of peaks of a tin-rich (red), stoichiometric (pink), and an A-rich film (violet). All films show the same threefold symmetry of the 400 family of peaks as the off-axis ϕ -scan of the 200 family of peaks of the substrate (black), confirming the epitaxial relationship between films and substrates. (c) Rocking curves of the 222 peak of $\text{La}_2\text{Sn}_2\text{O}_7$ films as a function of their Sn/La ratio given to the right.

oscillations are observed about the 222 diffraction peak. What is surprising, however, is that we are still able to observe all diffraction peaks except for the naturally least intense 111 peak. Together with the ϕ -scan, this reveals that the bulk of the film, below the polycrystalline surface, is still epitaxial $\text{La}_2\text{Sn}_2\text{O}_7$ with the pyrochlore structure.

Having established three distinct regimes of growth, the next step is to understand the mechanisms that differentiate them. In order to do this, we have to understand the accommodation of the cation non-stoichiometry and the accompanying defect chemistry.

Starting with stoichiometric growth in **regime I**, the high-quality of the surface and structural perfection suggest that the films are single-phase with minimal defects. While an increase in lanthanum still yields high-quality films, the additional lanthanum needs to be accommodated and the shift of the x-ray diffraction peaks to lower angles indicates a structural change. Considering the defect calculations for pyrochlores by Stanek *et al.*, the energetically favorable accommodation mechanism for A-site excess in pyrochlores is the formation of anti-site defects whose charge is compensated by oxygen vacancies.²⁵ The formation energy for anti-site defects in pyrochlores is generally low in comparison to other oxides such as perovskites as the ionic radii are usually similar (in the case of La^{3+} and Sn^{4+} 250 pm and 225 pm, respectively) and the crystal structure is less densely packed—often even resulting in anti-site defects without an applied off-stoichiometry.^{2,3,8} Applying this to $\text{La}_2\text{Sn}_2\text{O}_7$ results in Eq. (3) in Kröger-Vink notation,⁵⁹



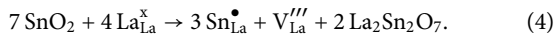
The additional lanthanum (here, given in its oxide form La_2O_3) forms an anti-site defect on a tin site, resulting in a single negative charge (La'_{Sn}). The charge of two such anti-site defects is compensated by a single oxygen vacancy ($\text{V}_{\text{O}}^{\bullet\bullet}$). These oxygen vacancies explain the shift toward lower angles in the diffraction pattern as they result in a lattice expansion.⁶⁰ Furthermore, the oxygen vacancies are one possible explanation for the decreasing intensity of the 111 and 333 peaks with increasing lanthanum content. A pyrochlore with an additional oxygen vacancy translates into a bixbyite-like structure where these peaks are forbidden. Li *et al.* on the other hand explained the diminishing intensity of what they refer to as the 111 pyrochlore super-lattice peak with a loss of the super-lattice order due to the anti-site defects, in principle, making the 222 fluorite-type peak the 111 peak of the material.⁶¹

One may be inclined to think that electrons may accompany the oxygen vacancies resulting from Eq. (3). This is not, however, the case. The oxygen vacancies compensate the charges arising from the acceptor-type lanthanum anti-site defects to precisely maintain charge neutrality and, thus, do not generate electrons. The accommodation of cation defects by oxygen vacancies is well known for other oxide crystal structures such as perovskites, i.e., ATiO_3 ,^{62,63} and LaBO_3 ,^{63,64} fluorites, i.e., CeO_2 ,⁶⁵ and YSZ ,⁶⁶ and bixbyites, i.e., In_2O_3 ,⁶⁷ and Y_2O_3 .⁶⁸

Upon further increasing the lanthanum ratio, we shift into growth **regime II**. The appearance of islands shows that we are reaching the solubility limit of lanthanum on the tin site. As a result, the expulsion of lanthanum becomes favorable. Underneath the islands, $\text{La}_2\text{Sn}_2\text{O}_7$ with the maximum thermodynamically allowed

lanthanum anti-site defect concentration grows; thus, these films also show the maximal 2θ peak shift in XRD.

In contrast to the ability of $\text{La}_2\text{Sn}_2\text{O}_7$ to accommodate surplus lanthanum, surplus tin in **regime III** seems hardly, if at all, soluble. While the defect calculations of Stanek *et al.* predict a *B*-site compensation by point defects,²⁵ which would translate to Eq. (4) for $\text{La}_2\text{Sn}_2\text{O}_7$, this seems not to be the main compensation mechanism in our thin films,



A possible reason for this can be found when considering the formation enthalpy of SnO_2 , which is low ($\Delta_f^0 H = -6.612$ eV/atom)³² when compared to La_2O_3 ($\Delta_f^0 H = -3.851$ eV/atom).⁶⁹ An expulsion of SnO_2 may, thus, be energetically more favorable for the system than compensation by point defects—shifting Eq. (4) to the left-hand side. This would also explain why, despite the surface roughening caused by the aforementioned expulsion, we still detect a near-stoichiometric $\text{La}_2\text{Sn}_2\text{O}_7$ diffraction pattern. Growing with a tin surplus results in the formation of stoichiometric $\text{La}_2\text{Sn}_2\text{O}_7$ with a small amount of additional tin forming anti-site defects, as given by Eq. (4), which are responsible for the small peak shift. Equation (4) is energetically biased to the left-hand side, however, resulting in the majority of the tin being expelled to the surface where it forms polycrystalline SnO_2 . This is confirmed by the position of the diffraction rings in the RHEED pattern in Fig. 1(c). As we know the lattice parameter of the underlying cubic phase, we can compare the distance of the cubic features to the distance of the polycrystalline features. This gives us a lattice parameter of 0.48 nm, reasonably matching that of polycrystalline SnO_2 ($a = 0.4738$ nm),⁷⁰ especially considering the blurry RHEED-features.

IV. ELECTRONIC STRUCTURE OF $\text{La}_2\text{Sn}_2\text{O}_7$

Having established a stable growth window for $\text{La}_2\text{Sn}_2\text{O}_7$, the next step is to try to achieve *n*-type conductivity by means of extrinsic doping. For SnO_2 , one of the most promising transparent conducting oxides, the most commonly used donor dopant is antimony, which occupies a tin site $\text{Sb}_{\text{Sn}}^{\bullet}$ and results in *n*-type conductivity.^{71,72} This motivated us to attempt to dope in $\text{La}_2\text{Sn}_2\text{O}_7$ with antimony hoping to substitute it onto the tin site and thus produce the desired *n*-type conductivity.

To achieve antimony doping in $\text{La}_2\text{Sn}_2\text{O}_7$, we successively decrease the flux of the SnO_2 source, while increasing the flux of the antimony source. We are able to achieve high-quality epitaxial thin films for antimony doping concentrations up to 20% ($\text{La}_2\text{Sn}_{1.6}\text{Sb}_{0.4}\text{O}_7$). This can be concluded from the corresponding θ - 2θ XRD scan in Fig. 4 in red. As established earlier in this article, the peak position and the thickness fringes are clear indicators for high-quality epitaxial $\text{La}_2\text{Sn}_2\text{O}_7$ thin films. Despite the high quality of the epitaxial antimony-doped thin films, no measurable conductivity is observed by two-point measurements using an ohmmeter, independent of the doping concentration of up to 20%.

To understand the lack of conductivity, we use first-principles defect computations using the HSE functional. A bandgap of 4.5 eV is computed for $\text{La}_2\text{Sn}_2\text{O}_7$. To validate this computed bandgap for the $\text{La}_2\text{Sn}_2\text{O}_7$ thin films, we performed spectroscopic ellipsometry on the stoichiometric sample. In divided spectral range analysis, the total measured spectral range is divided into

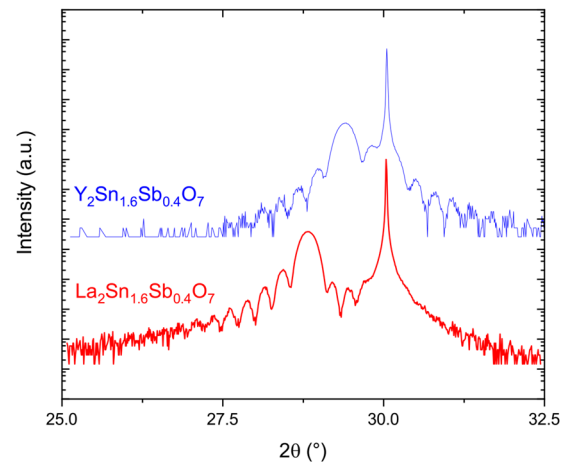


FIG. 4. Narrow-range diffraction pattern between $2\theta = 25^\circ$ and $2\theta = 32.5^\circ$ in the vicinity of the YSZ 111 substrate peak for 20% Sb-doped $\text{La}_2\text{Sn}_2\text{O}_7$ (red) and 20% Sb-doped $\text{Y}_2\text{Sn}_2\text{O}_7$ (blue).

three different regions corresponding to those that are nominally transparent, weakly absorbing, and highly absorbing. For $\text{La}_2\text{Sn}_2\text{O}_7$, the transparent region spans from 0.74 to 3.00 eV. For this region, spectra in ϵ are represented by a Sellmeier expression⁷³ and a constant additive contribution to the real part of ϵ is denoted as ϵ_∞ . The highly absorbing photon energy range is above the bandgap and extends from 4.52 to 5.89 eV. Spectra in ϵ in the highly absorbing region are parameterized using a critical point parabolic band (CPPB)⁷⁴ oscillator, a Sellmeier expression, and ϵ_∞ . Common structural parameters including surface roughness layer thickness, and bulk thickness of the film are fit in the simultaneous analysis of both the transparent and highly absorbing spectral ranges while fitting each region to its respective parametric model for ϵ . From the thicknesses obtained, numerical inversion⁷⁵ is used to extract ϵ over the full spectral range, as shown in Fig. 5. This approach using numerical inversion to obtain ϵ in the weakly absorbing region does not require imposing a particular parametric model bias in the vicinity of the bandgap. The bulk thickness of the $\text{La}_2\text{Sn}_2\text{O}_7$ thin film is determined to be 43.2 ± 0.5 nm with a corresponding surface roughness of 4.7 ± 0.2 nm. The thickness determined by spectroscopic ellipsometry is in agreement with that obtained on the same film by x-ray reflectivity, 45.13 ± 1.46 nm.

The absorption coefficient (α) spectra are obtained from $\alpha = \frac{4\pi k}{\lambda}$, where k is the extinction coefficient obtained from $\epsilon = (n + ik)^2$ and λ is the photon wavelength. Figure 6(a) shows α^2 as a function of photon energy for $\text{La}_2\text{Sn}_2\text{O}_7$. The direct bandgap is obtained via a Tauc plot by extrapolating the photon energy at which $\alpha^2 = 0$. The linear range of these extrapolations corresponds to α between 9.5×10^3 and 1.983×10^4 cm^{-1} . The direct bandgap energy measured for the stoichiometric $\text{La}_2\text{Sn}_2\text{O}_7$ thin film is, thus, 4.20 eV. This value is in reasonable agreement with the bandgap of 4.5 eV obtained by diffuse powder reflection by Mizoguchi *et al.*²⁶

The computed bandgap agrees very well with the experimental value and is within the typical errors between HSE and the

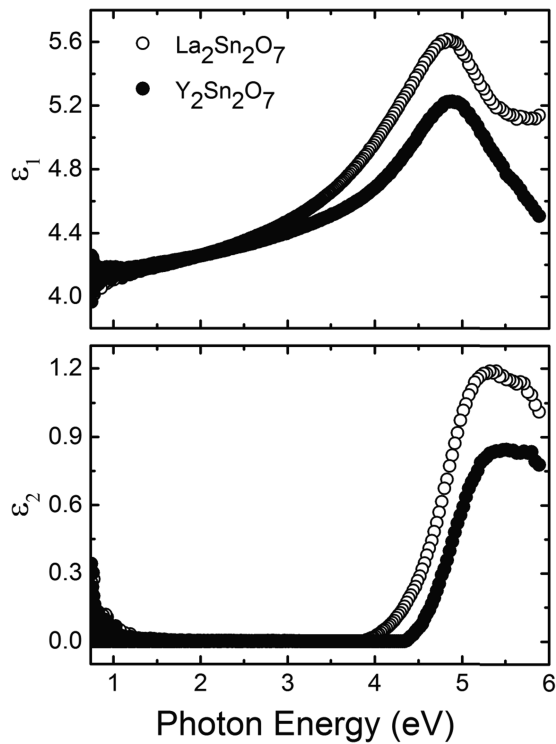


FIG. 5. Complex dielectric function ($\epsilon = \epsilon_1 + i\epsilon_2$) spectra obtained by divided spectral range analysis and numerical inversion for stoichiometric epitaxial $\text{La}_2\text{Sn}_2\text{O}_7$ (empty) and $\text{Y}_2\text{Sn}_2\text{O}_7$ (filled) films of thickness 43.2 ± 0.5 nm and 48.6 ± 0.2 nm, respectively.

experiment.⁷⁶ Previous calculations relied on local or semilocal functionals, which are known to significantly underestimate the bandgap. For example, 3.3–3.4 eV have been obtained using the local density approximation (LDA)^{15,26} and 2.7 eV using the generalized gradient approximation (GGA).⁷⁷

Given their precision, HSE hybrid computations are perfectly appropriate to study the dopant level of antimony substitutional defects and the oxygen vacancies in $\text{La}_2\text{Sn}_2\text{O}_7$. Figure 7(a) shows the formation energy of neutral (horizontal lines) and charged (non-horizontal lines) oxygen vacancies (blue and magenta for O and O', respectively) and antimony-on-tin substitutional defects (red) in cation-rich/anion-poor and cation-poor/anion-poor regions. While growth conditions can modify the chemical potential and, thus, the formation energy of the defects, the defect transition states between the neutral and charged states (+1 for Sb_{Sn} and +2 for the oxygen vacancy) are both quite far from the conduction band (0.4 eV and 1.9 eV, respectively), indicating that they are deep defects. Such defects can be present, but do not contribute significantly to the carrier concentration. This rationalizes why up to 20% antimony excess can be incorporated into the film without markedly affecting the electrical conductivity. Utilizing the Boltzmann distribution $N = N_d e^{-E_f/k_B T}$, where N_d is the number of possible defect sites, which is determined by the multiplicity of the defect's Wyckoff position, the concentration of carriers and defects is computed by imposing charge neutrality of

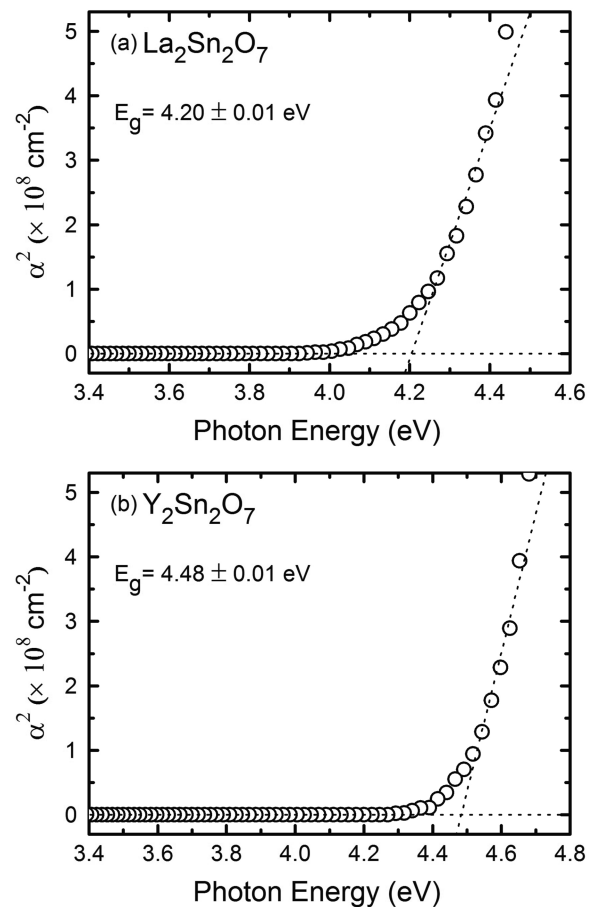


FIG. 6. α^2 as a function of photon energy to obtain the direct bandgap energies of stoichiometric epitaxial (a) $\text{La}_2\text{Sn}_2\text{O}_7$ and (b) $\text{Y}_2\text{Sn}_2\text{O}_7$ films.

the system at room temperature. In our model, which does not take into account compensation from other defects, for 20% antimony excess, this results in an electron concentration of at most 10^{16} cm^{-3} .

Although in SnO_2 the oxygen vacancy is also deep (located further than 0.2 eV from the bottom of the conduction band) where it contributes minimally to conductivity at room temperature, antimony is shallow (within 0.2 eV of the bottom of the conduction band) consistent with its effective use as an *n*-type dopant. The different behavior in $\text{La}_2\text{Sn}_2\text{O}_7$ can be linked to its higher bandgap, 4.5 eV for $\text{La}_2\text{Sn}_2\text{O}_7$ compared to 3.6 eV for SnO_2 , leading to deeper defects.⁷⁸

An alternative strategy for achieving *n*-type conductivity in SnO_2 has been to dope the anion site instead of the cation site with fluorine ($\text{F}_\text{O}^\bullet$).⁷⁹ We also explored this possibility computationally. Two distinct anion sites are found in pyrochlores. Figures 7(c) and 7(d) show the dopant levels of fluorine for both oxygen sites (red and green) for different growth conditions. The two oxygen sites behave differently leading to a deep and shallow $\text{F}_\text{O}^\bullet$ defect. The shallow defect formed by fluorine substitution on O' is a good candidate

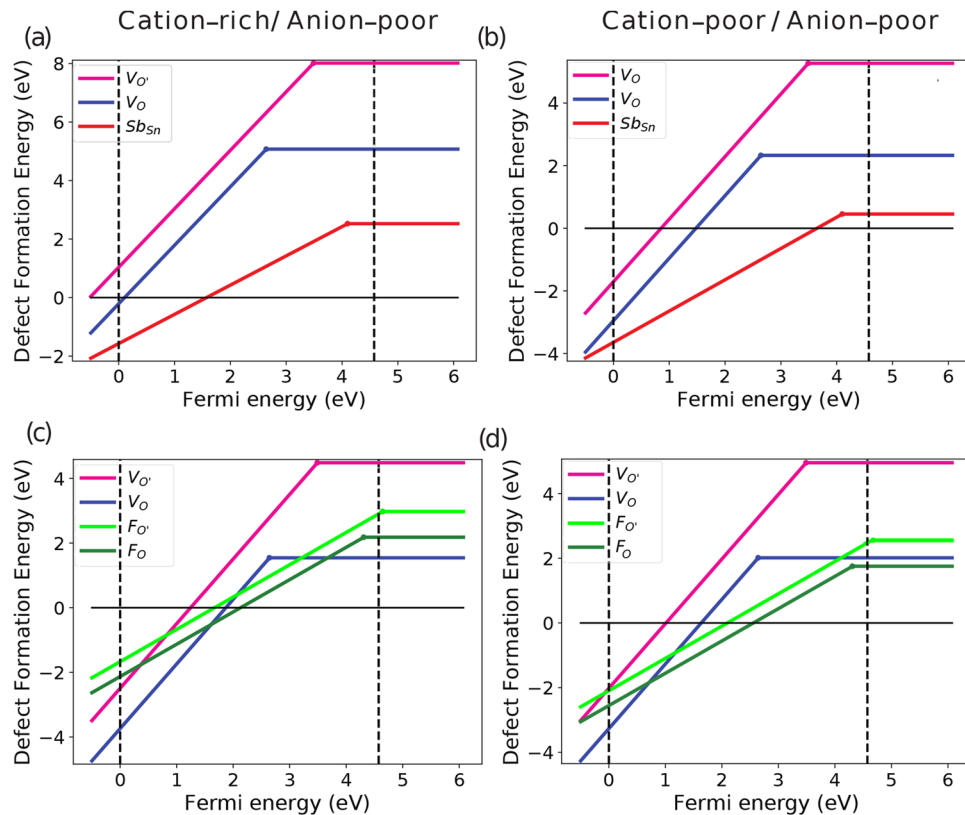


FIG. 7. The dependence of the defect formation energy on the Fermi energy for different growth conditions and dopants obtained by HSE computations. [(a) and (b)] Antimony doping on the tin site (red). [(c) and (d)] Fluorine doping on the oxygen site (green and red). The formation energy of oxygen vacancies is shown in magenta and blue. The different formation energies for anion site defects result from the two different coordination states of the anion in pyrochlores. The left and the right column each represents how growth-induced non-stoichiometry can influence the energy levels. The left column represents cation-rich and anion-poor conditions; the right column represents cation-poor and anion-poor conditions.

for n -type conductivity. Our computations indicate that a 5% substitution of oxygen by fluorine would lead to electron concentrations of 10^{18} cm^{-3} at room temperature.

V. APPLICATION TO $\text{Y}_2\text{Sn}_2\text{O}_7$

Next, we consider whether the results obtained for $\text{La}_2\text{Sn}_2\text{O}_7$ are equally applicable to other stannate pyrochlores. To this end, we have attempted the growth of $\text{Y}_2\text{Sn}_2\text{O}_7$.

In a similar way, as occurs for $\text{La}_2\text{Sn}_2\text{O}_7$, varying the cation ratio of $\text{Y}_2\text{Sn}_2\text{O}_7$ allows the limits of non-stoichiometry and the ideal stoichiometry to be established. Figure 8(a) shows the θ - 2θ XRD scan in the vicinity of the YSZ 111 substrate peak. The dashed line marks the 222 2θ value expected based on the bulk lattice constant of $\text{Y}_2\text{Sn}_2\text{O}_7$.³¹ The most tin-rich film (red) has the least defined peak and is the only one about which thickness fringes are absent. The peak of the film with a Sn/Y ratio of 0.89 (pink) obtained by QCM is closest to the expected bulk lattice constant, which means that this flux ratio results in the ideal stoichiometry. Upon increasing the Y-content of the films, the peak shifts to lower angles maintaining its thickness fringes, however, indicating

that good crystallinity and smooth surfaces are also maintained. The reciprocal space map of the 331 substrate peak and the 662 peak of the film with the lattice constant closest to the expected bulk value in Fig. 8(b) reveals that the film is compressively strained in-plane. This is in good agreement with the lattice mismatch between $\text{Y}_2\text{Sn}_2\text{O}_7$ and YSZ.

The change in the crystal structure underlying the shift of the $\text{Y}_2\text{Sn}_2\text{O}_7$ 222 peak is illustrated by the dependence of the out-of-plane lattice constant of the Sn/Y ratio in Fig. 3(a) (blue). It is obvious that the lattice constant nearest to the bulk value is not found for a cation ratio of 1, but for Sn/Y = 0.89. As the cation ratio is calculated from the fluxes obtained by QCM, this is likely a result of the inaccuracy of this calibration method. Noticeably, the out-of-plane lattice constant is also larger than its bulk counterpart³¹ even for our point of ideal stoichiometry. This is in good agreement with the in-plane compressive strain, resulting in an out-of-plane lattice constant elongation.

Strong similarities are apparent in the structural data obtained for $\text{Y}_2\text{Sn}_2\text{O}_7$ and $\text{La}_2\text{Sn}_2\text{O}_7$ films. For both stannate pyrochlores, tin-excess results in the loss of thickness fringes about the 222 peak. In addition, A-site excess can be accommodated in both without

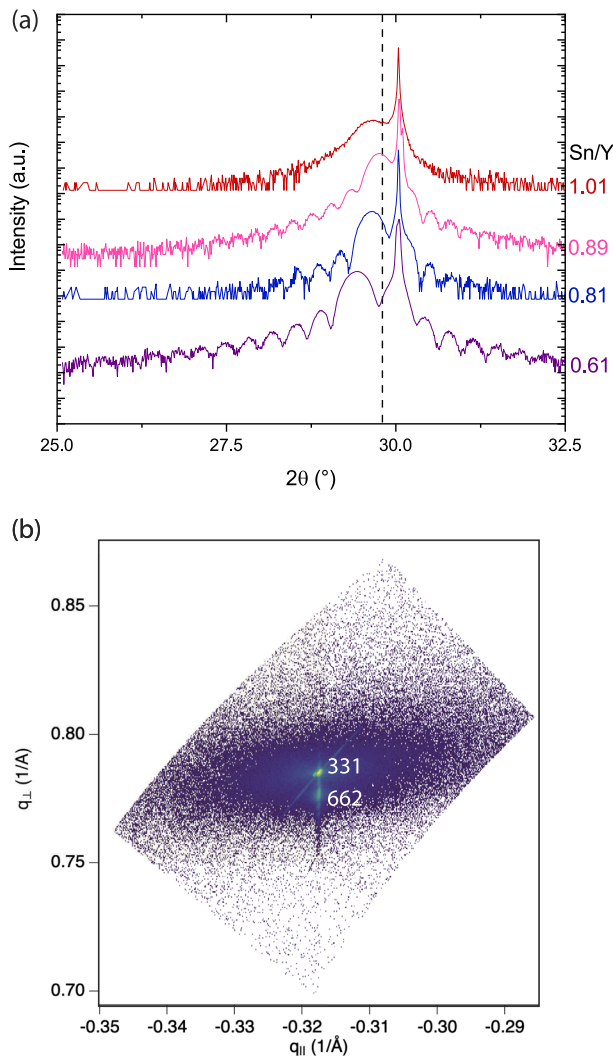
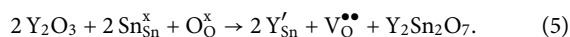


FIG. 8. (a) Narrow-range diffraction patterns between $2\theta = 25^\circ$ and $2\theta = 32.5^\circ$ in the vicinity of the YSZ 111 substrate peak for $Y_2Sn_2O_7$ with different Sn/Y-ratios. The dashed line marks the expected diffraction angle of the 222 peak of $Y_2Sn_2O_7$ based on the bulk lattice constant.³¹ (b) Reciprocal space map of the 331 substrate peak and the 662 film peak of the film with a cation ratio Sn/Y of 0.89.

a significant loss of crystalline quality. In an analogous manner to $La_2Sn_2O_7$, we can explain the accommodation of *A*-site excess in $Y_2Sn_2O_7$ by the formation of anti-site defects,



The lack of tin accommodation can again be explained by the low formation enthalpy of SnO_2 .

Having established the point of ideal stoichiometry, the next step was to attempt to achieve *n*-type conductivity by means of antimony doping. Figure 4(a) (blue) reveals that, similar to $La_2Sn_2O_7$, we can maintain high crystal quality for antimony doping concentrations of up to 20% ($Y_2Sn_{1.6}Sb_{0.4}O_7$). Unfortunately, we do not observe conductivity despite the high crystalline quality.

In this article, we demonstrated that HSE hybrid computations are a precise method to calculate the bandgap and dopant level for $La_2Sn_2O_7$. This enables us to utilize the more accessible GGA computations for $Y_2Sn_2O_7$ while maintaining a realistic estimation of the precision. HSE hybrid computations revealed the dopant level of antimony to be 0.4 eV below the bottom of the conduction band of $La_2Sn_2O_7$ as discussed above. GGA computations wrongly place the energy of the dopant level above the bottom of the conduction band. For $Y_2Sn_2O_7$, however, GGA computations reveal the antimony dopant level to be 0.25 eV below the bottom of the conduction band. It is reasonable to assume that the real dopant level of antimony will be even deeper. It is, thus, not surprising that antimony doping of $Y_2Sn_2O_7$ does also not yield *n*-type conductivity.

This is supported by our observations from spectroscopic ellipsometry performed on the $Y_2Sn_2O_7$ thin film identified as stoichiometric. Using the same approach of divided spectral analysis (Fig. 5) as for $La_2Sn_2O_7$, but with a transparent region from 0.74 to 3.6 eV and a highly absorbing region from 4.76 to 5.89 eV, the bulk thickness is determined to be 48.6 ± 0.2 nm with a surface roughness of 6.2 ± 0.1 nm. Again, the thickness determined by spectroscopic ellipsometry is in agreement with that determined on the same film by x-ray reflectivity, 44.49 ± 0.87 nm. The direct bandgap determined from Fig. 6(b) is 4.48 eV and, thus, even higher than that of $La_2Sn_2O_7$ (4.20 eV). This larger bandgap suggests that the antimony-tin defect will not be shallower in $Y_2Sn_2O_7$.

VI. SUMMARY

In conclusion, we have established the cation stoichiometry window within which stannate pyrochlores can be grown epitaxially with high crystalline quality. We find that it is possible to induce a significant *A*-site surplus into both $La_2Sn_2O_7$ and $Y_2Sn_2O_7$, without forming a second phase. The incorporated excess results in a shift of the XRD peaks to lower 2θ due to the point defects incorporated. We have established that this *A*-site surplus results in the formation of anti-site defects and oxygen vacancies. Once the solubility limit is reached, additional *A*-site surplus is expelled. On the other hand, the concentration of excess tin that can be incorporated into $La_2Sn_2O_7$ and $Y_2Sn_2O_7$ is very small. Even a tiny tin surplus is expelled due to the low formation enthalpy of SnO_2 .

The bandgap of $La_2Sn_2O_7$ calculated by HSE hybrid computations is in good agreement with the experimental value obtained by spectroscopic ellipsometry. This contrasts with previous bandgap calculations, which used methods known to underestimate the bandgap: the underestimation was especially severe for pyrochlores. This explains why achieving *n*-type conductivity in stannate pyrochlores is more challenging than previously assumed.^{14,15,26} More specifically, we showed that antimony doping even to very high levels does not lead to *n*-type as the antimony-on-tin defect lies deep within the bandgap. Computational results indicate that fluorine doping might be more promising to reach *n*-type conductivity as fluorine on oxygen will lead to shallow defects.

Our results further pave the way for future thin film applications of the highly interesting stannate pyrochlores. The possibility of high-quality epitaxial thin films with a controllable defect structure is especially interesting for their applications in the field of

catalysis. Fluorine doping of stannate pyrochlores could provide a route to a new type of transparent conducting oxide and even lay the basis for an exotic superconducting heterostructure.

ACKNOWLEDGMENTS

F.V.E.H., P.S., J.S., H.P., and D.G.S. acknowledge the support from the National Science Foundation [Platform for the Accelerated Realization, Analysis, and Discovery of Interface Materials (PARADIM)] under Cooperative Agreement No. DMR-1539918. Substrate preparation was performed, in part, at the Cornell NanoScale Facility, a member of the National Nanotechnology Coordinated Infrastructure (NNCI), which is supported by the National Science Foundation (NSF, Grant No. ECCS-1542081). This work made use of the CESI shared facilities, which is supported by the National Science Foundation (NSF, Grant No. MRI DMR-1338010) and the Kavli Institute at Cornell. D.D. was funded by the Conseil de l'action internationale (CAI) through a doctorate grant "Coopération au Développement." The authors acknowledge access to various computational resources. The present research benefited from computational resources made available on the Tier-1 supercomputer of the Fédération Wallonie-Bruxelles, infrastructure funded by the Walloon Region under Grant Agreement No. 1117545. Computational resources have been provided by the supercomputing facilities of the Université catholique de Louvain (CISM/UCL) and the Consortium des Équipements de Calcul Intensif en Fédération Wallonie Bruxelles (CÉCI) funded by the Fond de la Recherche Scientifique de Belgique (F.R.S.-FNRS) under convention 2.5020.11 and by the Walloon Region.

F.V.E.H. acknowledges funding from the Alexander von Humboldt Foundation in the form of a Feodor Lynen fellowship.

The authors declare no competing interest.

DATA AVAILABILITY

The data supporting the findings of this study are available within the paper. Additional data related to the growth and structural characterization are available at 10.34863/pvfm-0y37. Any additional data connected to the study are available from the corresponding author upon reasonable request.

REFERENCES

- C. N. R. Rao, "Transition metal oxides," *Annu. Rev. Phys. Chem.* **40**, 291–326 (1989).
- M. A. Subramanian, G. Aravamudan, and G. V. Subba Rao, "Oxide pyrochlores—A review," *Prog. Solid State Chem.* **15**, 55 (1983).
- L. Minervini, R. W. Grimes, and K. E. Sickafus, "Disorder in pyrochlore oxides," *J. Am. Ceram. Soc.* **83**, 1873–1878 (2000).
- W. Ren, S. Trolier-McKinstry, C. A. Randall, and T. R. Shrout, "Bismuth zinc niobate pyrochlore dielectric thin films for capacitive applications," *J. Appl. Phys.* **89**, 767–774 (2001).
- M. Valant and P. K. Davies, "Crystal chemistry and dielectric properties of chemically substituted $(\text{Bi}_{1.5}\text{Zn}_{1.0}\text{Nb}_{1.5})\text{O}_7$ and $\text{Bi}_2(\text{Zn}_{2/3}\text{Nb}_{4/3})\text{O}_7$ pyrochlores," *J. Am. Ceram. Soc.* **83**, 147–153 (2000).
- X. Wang, H. Wang, and X. Yao, "Structures, phase transformations, and dielectric properties of pyrochlores containing bismuth," *J. Am. Ceram. Soc.* **80**, 2745–2748 (2005).
- D. P. Cann, C. A. Randall, and T. R. Shrout, "Investigation of the dielectric properties of bismuth pyrochlores," *Solid State Commun.* **100**, 529–534 (1996).
- K. E. Sickafus, L. Minervini, R. W. Grimes, J. A. Valdez, M. Ishimaru, F. Li, K. J. McClellan, and T. Hartmann, "Radiation tolerance of complex oxides," *Science* **289**, 748–751 (2000).
- C. Childs, K. V. Lawler, A. L. Hector, S. Petitgirard, O. Noked, J. S. Smith, D. Daisenberger, L. Bezacier, M. Jura, C. J. Pickard, and A. Salamat, "Covalency is frustrating: $\text{La}_2\text{Sn}_2\text{O}_7$ and the nature of bonding in pyrochlores under high pressure-temperature conditions," *Inorg. Chem.* **57**, 15051–15061 (2018).
- S. H. Oh, R. Black, E. Pomerantseva, J.-H. Lee, and L. F. Nazar, "Synthesis of a metallic mesoporous pyrochlore as a catalyst for lithium- O_2 batteries," *Nat. Chem.* **4**, 1004–1010 (2012).
- D. Haynes, D. Berry, D. Shekhawat, and J. Spivey, "Catalytic partial oxidation of n-tetradecane using pyrochlores: Effect of Rh and Sr substitution," *Catal. Today* **136**, 206–213 (2008).
- M. Kim, J. Park, M. Kang, J. Y. Kim, and S. W. Lee, "Toward efficient electrocatalytic oxygen evolution: Emerging opportunities with metallic pyrochlore oxides for electrocatalysts and conductive supports," *ACS Cent. Sci.* **6**, 880–891 (2020).
- L. Miao, Y. Lee, A. B. Mei, M. J. Lawler, and K. M. Shen, "Two-dimensional magnetic monopole gas in an oxide heterostructure," *Nat. Commun.* **11**, 1341 (2020).
- J.-H. She, C. H. Kim, C. J. Fennie, M. J. Lawler, and E.-A. Kim, "Topological superconductivity in metal/quantum-spin-ice heterostructures," *npj Quantum Mater.* **2**, 64 (2017); [arXiv:1603.02692](https://arxiv.org/abs/1603.02692).
- Y. Zhao, N. Li, C. Xu, Y. Li, H. Zhu, P. Zhu, X. Wang, and W. Yang, "Abnormal pressure-induced photoluminescence enhancement and phase decomposition in pyrochlore $\text{La}_2\text{Sn}_2\text{O}_7$," *Adv. Mater.* **29**, 1701513 (2017).
- S. Park, H. J. Hwang, and J. Moon, "Catalytic combustion of methane over rare earth stannate pyrochlore," *Catal. Lett.* **87**, 219–223 (2003).
- J. Cheng, H. Wang, Z. Hao, and S. Wang, "Catalytic combustion of methane over cobalt doped lanthanum stannate pyrochlore oxide," *Catal. Commun.* **9**, 690–695 (2008).
- Y. Ma, X. Wang, X. You, J. Liu, J. Tian, X. Xu, H. Peng, W. Liu, C. Li, W. Zhou, P. Yuan, and X. Chen, "Nickel-supported on $\text{La}_2\text{Sn}_2\text{O}_7$ and $\text{La}_2\text{Zr}_2\text{O}_7$ pyrochlores for methane steam reforming: Insight into the difference between tin and zirconium in the B site of the compound," *ChemCatChem* **6**, 3366–3376 (2015).
- J. Zeng, H. Wang, Y. Zhang, M. K. Zhu, and H. Yan, "Hydrothermal synthesis and photocatalytic properties of pyrochlore $\text{La}_2\text{Sn}_2\text{O}_7$ nanocubes," *J. Phys. Chem. C* **111**, 11879–11887 (2007).
- S. Chen, B. Pan, L. Zeng, S. Luo, X. Wang, and W. Su, " $\text{La}_2\text{Sn}_2\text{O}_7$ enhanced photocatalytic CO_2 reduction with H_2O by deposition of Au co-catalyst," *RSC Adv.* **7**, 14186–14191 (2017).
- J.-y. Yang, Y.-c. Su, and X.-y. Liu, "Hydrothermal synthesis, characterization and optical properties of $\text{La}_2\text{Sn}_2\text{O}_7$: Eu^{3+} micro-octahedra," *Trans. Nonferrous Met. Soc. China* **21**, 535–543 (2011).
- C. J. Eom, D. Y. Kuo, C. Adamo, E. J. Moon, S. J. May, E. J. Crumlin, D. G. Schlom, and J. Suntivich, "Tailoring manganese oxide with atomic precision to increase surface site availability for oxygen reduction catalysis," *Nat. Commun.* **9**, 4034 (2018).
- M. L. Weber and F. Gunkel, "Epitaxial catalysts for oxygen evolution reaction: Model systems and beyond," *J. Phys.: Energy* **1**, 031001 (2019).
- J. Scholz, M. Risch, G. Wartner, C. Luderer, V. Roddatis, and C. Jooss, "Tailoring the oxygen evolution activity and stability using defect chemistry," *Catalysts* **7**, 15–19 (2017).
- C. R. Stanek, L. Minervini, and R. W. Grimes, "Nonstoichiometry in $\text{A}_2\text{B}_2\text{O}_7$ pyrochlores," *J. Am. Ceram. Soc.* **85**, 2792–2798 (2004).
- H. Mizoguchi, H. W. Eng, and P. M. Woodward, "Probing the electronic structures of ternary perovskite and pyrochlore oxides containing Sn^{4+} or Sb^{5+} ," *Inorg. Chem.* **43**, 1667–1680 (2004).
- Z. Lu, J. Wang, Y. Tang, and Y. Li, "Synthesis and photoluminescence of Eu^{3+} -doped $\text{Y}_2\text{Sn}_2\text{O}_7$ nanocrystals," *J. Solid State Chem.* **177**, 3075–3079 (2004).
- A. M. Srivastava, "On the luminescence of Bi^{3+} in the pyrochlore $\text{Y}_2\text{Sn}_2\text{O}_7$," *Mater. Res. Bull.* **37**, 745–751 (2002).
- K. Li, H. Wang, and H. Yan, "Hydrothermal preparation and photocatalytic properties of $\text{Y}_2\text{Sn}_2\text{O}_7$ nanocrystals," *J. Mol. Catal. A: Chem.* **249**, 65–70 (2006).

- ³⁰B. J. Kennedy, "Structural trends in pyrochlore oxides," *Mater. Sci. Forum* **228-231**, 753–758 (1996).
- ³¹G. R. Facer, C. J. Howard, and B. J. Kennedy, "Structure refinement and calculated X-ray powder data for the pyrochlore $Y_2Sn_2O_7$ derived from powder neutron data," *Powder Diffr.* **8**, 245–248 (1993).
- ³²H. Paik, Z. Chen, E. Lochocki, A. Seidner H., A. Verma, N. Tanen, J. Park, M. Uchida, S. Shang, B.-C. Zhou, M. Brützmam, R. Uecker, Z.-K. Liu, D. Jena, K. M. Shen, D. A. Muller, and D. G. Schlom, "Adsorption-controlled growth of La-doped $BaSnO_3$ by molecular-beam epitaxy," *APL Mater.* **5**, 116107 (2017).
- ³³K. M. Adkison, S.-L. Shang, B. J. Bocklund, D. Klimm, D. G. Schlom, and Z.-K. Liu, "Suitability of binary oxides for molecular-beam epitaxy source materials: A comprehensive thermodynamic analysis," *APL Mater.* **8**, 081110 (2020).
- ³⁴G. Hoffmann, M. Budde, P. Mazzolini, and O. Bierwagen, "Efficient suboxide sources in oxide molecular beam epitaxy using mixed metal + oxide charges: The examples of SnO and Ga_2O_3 ," *APL Mater.* **8**, 031110 (2020).
- ³⁵P. E. Blöchl, "Projector augmented-wave method," *Phys. Rev. B* **50**, 17953–17979 (1994).
- ³⁶G. Kresse and J. Furthmüller, "Efficient iterative schemes for ab initio total-energy calculations using a plane-wave basis set," *Phys. Rev. B* **54**, 11169–11186 (1996).
- ³⁷G. Kresse and J. Furthmüller, "Efficiency of ab-initio total energy calculations for metals and semiconductors using a plane-wave basis set," *Comput. Mater. Sci.* **6**, 15–50 (1996).
- ³⁸C. Freysoldt, B. Grabowski, T. Hickel, J. Neugebauer, G. Kresse, A. Janotti, and C. G. Van de Walle, "First-principles calculations for point defects in solids," *Rev. Mod. Phys.* **86**, 253–305 (2014).
- ³⁹D. Broberg, B. Medasani, N. E. R. Zimmermann, G. Yu, A. Canning, M. Haranczyk, M. Asta, and G. Hautier, "PyCDT: A Python toolkit for modeling point defects in semiconductors and insulators," *Comput. Phys. Commun.* **226**, 165–179 (2018); [arXiv:1611.07481](https://arxiv.org/abs/1611.07481).
- ⁴⁰J. Heyd, G. E. Scuseria, and M. Ernzerhof, "Hybrid functionals based on a screened Coulomb potential," *J. Chem. Phys.* **118**, 8207–8215 (2003).
- ⁴¹J. L. Lyons and C. G. Van de Walle, "Computationally predicted energies and properties of defects in GaN," *npj Comput. Mater.* **3**, 12 (2017).
- ⁴²S. Zhang and J. Northrup, "Chemical potential dependence of defect formation energies in GaAs: Application to Ga self-diffusion," *Phys. Rev. Lett.* **67**, 2339–2342 (1991).
- ⁴³H. P. Komsa, T. T. Rantala, and A. Pasquarello, "Finite-size supercell correction schemes for charged defect calculations," *Phys. Rev. B* **86**, 1–16 (2012).
- ⁴⁴C. Freysoldt, J. Neugebauer, and C. G. Van de Walle, "Electrostatic interactions between charged defects in supercells," *Phys. Status Solidi B* **248**, 1067–1076 (2011).
- ⁴⁵Y. Kumagai and F. Oba, "Electrostatics-based finite-size corrections for first-principles point defect calculations," *Phys. Rev. B* **89**, 19205 (2014); [arXiv:1402.1226](https://arxiv.org/abs/1402.1226).
- ⁴⁶J. A. Woollam, B. D. Johs, C. M. Herzinger, J. N. Hilfiker, R. A. Synowicki, and C. L. Bungay, "Overview of variable-angle spectroscopic ellipsometry (VASE): I. Basic theory and typical applications," *Opt. Metrol.* **10294**, 1029402 (1999).
- ⁴⁷J. Lee, P. I. Rovira, I. An, and R. W. Collins, "Rotating-compensator multichannel ellipsometry: Applications for real time Stokes vector spectroscopy of thin film growth," *Rev. Sci. Instrum.* **69**, 1800–1810 (1998).
- ⁴⁸L. Karki Gautam, H. Haneef, M. M. Junda, D. B. Saint John, and N. J. Podraza, "Approach for extracting complex dielectric function spectra in weakly-absorbing regions," *Thin Solid Films* **571**, 548–553 (2014).
- ⁴⁹B. Subedi, L. Guan, Y. Yu, K. Ghimire, P. Uprety, Y. Yan, and N. J. Podraza, "Formamidinium + cesium lead triiodide perovskites: Discrepancies between thin film optical absorption and solar cell efficiency," *Sol. Energy Mater. Sol. Cells* **188**, 228–233 (2018).
- ⁵⁰D. E. Aspnes, J. B. Theeten, and F. Hottier, "Investigation of effective-medium models of microscopic surface roughness by spectroscopic ellipsometry," *Phys. Rev. B* **20**, 3292–3302 (1979).
- ⁵¹H. Fujiwara, J. Koh, P. I. Rovira, and R. W. Collins, "Assessment of effective-medium theories in the analysis of nucleation and microscopic surface roughness evolution for semiconductor thin films," *Phys. Rev. B* **61**, 10832–10844 (2000).
- ⁵²C. M. Brooks, L. F. Kourkoutis, T. Heeg, J. Schubert, D. A. Muller, and D. G. Schlom, "Growth of homoepitaxial $SrTiO_3$ thin films by molecular-beam epitaxy," *Appl. Phys. Lett.* **94**, 162905 (2009).
- ⁵³B. Jalan, P. Moetakef, and S. Stemmer, "Molecular beam epitaxy of $SrTiO_3$ with a growth window," *Appl. Phys. Lett.* **95**, 032906 (2009).
- ⁵⁴L. Qiao, T. C. Droubay, T. Varga, M. E. Bowden, V. Shutthanandan, Z. Zhu, T. C. Kaspar, and S. A. Chambers, "Epitaxial growth, structure, and intermixing at the $LaAlO_3/SrTiO_3$ interface as the film stoichiometry is varied," *Phys. Rev. B* **83**, 085408 (2011).
- ⁵⁵D. Han, M. Bouras, C. Botella, A. Benamrouche, B. Canut, G. Grenet, G. Saint-Girons, and R. Bachelet, "Structural properties of strained epitaxial $La_{1+\delta}CrO_3$ thin films," *J. Vac. Sci. Technol. A* **37**, 021512 (2019).
- ⁵⁶A. Prakash, P. Xu, X. Wu, G. Haugstad, X. Wang, and B. Jalan, "Adsorption-controlled growth and the influence of stoichiometry on electronic transport in hybrid molecular beam epitaxy-grown $BaSnO_3$ films," *J. Mater. Chem. C* **5**, 5730–5736 (2017).
- ⁵⁷J. A. Moyer, R. Misra, J. A. Mundy, C. M. Brooks, J. T. Heron, D. A. Muller, D. G. Schlom, and P. Schiffer, "Intrinsic magnetic properties of hexagonal $LuFeO_3$ and the effects of nonstoichiometry," *APL Mater.* **2**, 012106 (2014).
- ⁵⁸D. Ferrón, E. Langenberg, E. Ferreiro-Villa, E. Smith, C. Stafin, G. Catalan, N. Domingo, D. G. Schlom, and F. Rivadulla, "Deconvolution of phonon scattering by ferroelectric domain Walls and point defects in compositionally graded $PbTiO_3$ thin films," [arXiv:2104.14494](https://arxiv.org/abs/2104.14494) (2021).
- ⁵⁹F. A. Kröger and H. J. Vink, "Relations between the concentrations of imperfections in crystalline solids," *Solid State Phys.* **3**, 307–435 (1956).
- ⁶⁰G. Sala, M. J. Gutmann, D. Prabhakaran, D. Pomaranski, C. Mitchelitis, J. B. Kycia, D. G. Porter, C. Castelnovo, and J. P. Goff, "Vacancy defects and monopole dynamics in oxygen-deficient pyrochlores," *Nat. Mater.* **13**, 488–493 (2014).
- ⁶¹Y. H. Li, B. P. Uberuaga, C. Jiang, S. Choudhury, J. A. Valdez, M. K. Patel, J. Won, Y. Q. Wang, M. Tang, D. J. Safarik, D. D. Byler, K. J. McClellan, I. O. Usov, T. Hartmann, G. Baldinozzi, and K. E. Sickafus, "Role of antisite disorder on preamorphization swelling in titanate pyrochlores," *Phys. Rev. Lett.* **108**, 195504 (2012).
- ⁶²R. Moos, W. Menesklou, and K. H. Härdtl, "Hall-mobility of undoped N-type conducting strontium-titanate single-crystals between 19-K and 1373-K," *Appl. Phys. A* **61**, 389–395 (1995).
- ⁶³S. Aggarwal and R. Ramesh, "Point defect chemistry of metal oxide heterostructures," *Annu. Rev. Mat. Sci.* **28**, 463–499 (1998).
- ⁶⁴D. Lybye, F. W. Poulsen, and M. Mogensen, "Conductivity of A- and B-site doped $LaAlO_3$, $LaGaO_3$, $LaScO_3$ and $LaInO_3$ perovskites," *Solid State Ionics* **128**, 91–103 (2000).
- ⁶⁵J. Janek, M. Martin, and K. D. Becker, "Physical chemistry of solids—The science behind materials engineering," *Phys. Chem. Chem. Phys.* **11**, 3010 (2009).
- ⁶⁶K. Sasaki, J. Claus, and J. Maier, "Defect chemistry of oxides in partially frozen-in states: Case studies for $ZrO_2(Y_2O_3)$, $SrZrO_3(Y_2O_3)$, and $SrTiO_3$," *Solid State Ionics* **121**, 51–60 (1999).
- ⁶⁷J. H. W. De Wit, "Structural aspects and defect chemistry in In_2O_3 ," *J. Solid State Chem.* **20**, 143–148 (1977).
- ⁶⁸P.-L. Chen and I.-W. Chen, "Grain boundary mobility in Y_2O_3 : Defect mechanism and dopant effects," *J. Am. Ceram. Soc.* **79**, 1801–1809 (1996).
- ⁶⁹M. Zinkevich, S. Geupel, F. Aldinger, A. Durygin, S. K. Saxena, M. Yang, and Z.-K. Liu, "Phase diagram and thermodynamics of the La_2O_3 - Ga_2O_3 system revisited," *J. Phys. Chem. Solids* **67**, 1901–1907 (2006).
- ⁷⁰W. H. Baur and A. A. Khan, "Rutile-type compounds. IV. SiO_2 , GeO_2 and a comparison with other rutile-type structures," *Acta Crystallogr., Sect. B* **27**, 2133–2139 (1971).
- ⁷¹T. Minami, "Present status of transparent conducting oxide thin-film development for Indium-Tin-Oxide (ITO) substitutes," *Thin Solid Films* **516**, 5822–5828 (2008).
- ⁷²J. Maier and W. Göpel, "Investigations of the bulk defect chemistry of polycrystalline Tin(IV) oxide," *J. Solid State Chem.* **72**, 293–302 (1988).
- ⁷³R. W. Collins and A. S. Ferlauto, "Optical physics of materials," *ChemInform* **37**, 125 (2006).
- ⁷⁴D. E. Aspnes, "Handbook on semiconductors," in *Handbook on Semiconductors*, edited by M. Balkanski (North-Holland, Amsterdam, 1980), Vol. 2, p. 109.

⁷⁵W. G. Oldham, "Numerical techniques for the analysis of lossy films," *Surf. Sci.* **16**, 97–103 (1969).

⁷⁶M. K. Chan and G. Ceder, "Efficient band gap prediction for solids," *Phys. Rev. Lett.* **105**, 196403 (2010).

⁷⁷A. Jain, S. P. Ong, G. Hautier, W. Chen, W. D. Richards, S. Dacek, S. Cholia, D. Gunter, D. Skinner, G. Ceder, and K. A. Persson, "Commentary: The materials

project: A materials genome approach to accelerating materials innovation," *APL Mater.* **1**, 011002 (2013).

⁷⁸D. O. Scanlon and G. W. Watson, "On the possibility of p-type SnO₂," *J. Mater. Chem.* **22**, 25236–25245 (2012).

⁷⁹R. G. Gordon, "Criteria for choosing transparent conductors," *MRS Bull.* **25**, 52–57 (2000).